Metallogr. Microstruct. Anal. (2012) 1:106–114
DOI 10.1007/s13632-012-0019-7

TECHNICAL ARTICLE

Fracture Modes and Mechanical Characteristics of Machinable Brass Rods

George A. Pantazopoulos · Anagnostis I. Toulfatzis

Received: 20 April 2012 / Accepted: 26 July 2012 / Published online: 15 August 2012

Abstract Machinable brasses are a broad class of high strength copper–zinc alloys mainly containing lead to improve machinability. Conventional leaded brasses are widely used in several manufacturing sectors (i.e., fabrication of hydraulic components, fittings, valves, etc.) due to their superior workability in extrusion and drawing, together with their superior machinability for high efficiency production of final components in high speed/high precision machining centers. In addition to machinability, the mechanical behavior and general fracture mechanisms of these alloys are also important, due to their impact on the overall reliability and safety of brass components. In this study, the main fracture modes and mechanical characteristics of two industrial copper alloys, namely, CuZn39Pb3 and CuZn36Pb2As, are presented in relation to their microstructure. Optical metallography, macro- and microfractography, together with static and dynamic mechanical testing, were used as the principal analytical techniques for the present investigation.

Keywords Macrofractography · Microfractography · Machinable brass · Mechanical testing

Introduction

Brass rods, possessing sufficient mechanical strength, high workability, superior corrosion, and wear resistance, constitute an attractive class of materials with a wide spectrum of applications. Machinable brasses are manufactured by hot extrusion and cold drawing, and serve as raw materials for the production of a broad range of products, such as bolts, nuts, electrical connectors, valve bodies, and hydraulic fittings. The production of the final components involves various cutting operations, such as drilling, milling, and turning, typically performed using high speed machining processes. The machinability of those materials is a function of a complex combination of several material parameters, including phase and microstructure, second-phase particles size and distribution, and overall mechanical properties. Improved machinability minimizes tool wear and allows for the production of high precision components, exhibiting superior surface finish. Machinability/microstructure relationships, together with some reference of the mechanical properties of leaded brass alloys, have been previously studied and presented in the relevant literature [1–4]. The evaluation of mechanical properties and the relevant fracture mechanisms of machinable brass rods is a valuable subject for investigation, as the mechanical performance of brass components impacts the reliability and safety of the entire system. In the present comparison study, the mechanical characteristics of two brass alloys, namely, CuZn39Pb3 and CuZn36Pb2As, under static and dynamic loading, together with the respective failure mechanisms are highlighted. Alloy CuZn39Pb3 possesses maximum machinability for free cutting applications, while CuZn36Pb2As exhibits inferior machining properties, but combines high cold workability with excellent corrosion and dezincification resistance. These specific alloys, which belong to the same class of machinable brasses, were chosen due to their extensive use in industry, specifically in the manufacturing of critical hydraulic components, such as fittings and valves for water distribution circuits. An improved understanding

G. A. Pantazopoulos (✉) · A. I. Toulfatzis
ELKEME Hellenic Research Centre for Metals S.A.,
252 Piraeus Str., 17778 Athens, Greece
e-mail: gpantaz@halcor.vionet.gr

of the mechanisms which govern the deformation, and ultimately the fracture, of these materials would be helpful in optimizing the manufacturing operations and in identifying the principal failure processes that are responsible for the damage of these critical equipment components.

Experimental

The leaded brass alloy rods selected for the comparison evaluation were CuZn39Pb3 (CW614N) and CuZn36Pb2As (CW602N); nominal diameter was 22 mm. Alloy composition, as determined by optical emission spectrometry (OES) is shown in Table 1; both alloys are in compliance with the EN 12164 standard.

Low-magnification observations of surface and fracture morphology were performed using a stereomicroscope. Microstructural and morphological characterization was conducted on transverse cross sections after wet grinding, polishing, and immersion chemical etching in standard $FeCl_3$ solution for approximately 5 s at room temperature. The etching solution consists of a mixture of approximately 8 g $FeCl_3$, 10 mL HCl (aqueous solution 37 wt.%), and 90 mL de-ionized water. Metallographic evaluation was performed using an inverted optical microscope equipped with image analysis software for particle size and phase (area) fraction measurements. High-magnification observations of the microstructures and fracture surfaces were conducted on ultrasonically cleaned specimens, with a scanning electron microscope using both secondary electron (SE) and back-scattered electron (BSE) signals. Energy dispersive spectroscopy was used for selected area elemental chemical analysis. Tensile testing was performed in triplicate for each heat treatment condition, according to the EN 10002-1 standard. Tensile elongation measurements were carried out using a standard 50 mm gage length (referred as A50). Hardness testing was conducted using a 1 kg (9,807 Newton) applied load, according to BS EN ISO 6507-1. Hardness testing was performed at the midway areas of transverse sections (Ø22 mm) as dictated by relevant specifications and standard practice. Dynamic bending loading was performed on notched specimens (square section 10 × 10 mm^2 and 55 mm length) according to EN10045-1 standard (Charpy V-notch test). All mechanical tests were carried out using triplicate samples; the maximum standard error was lower than the permissible limit dictated by the relevant standard.

Results and Discussion

Microstructure

The typical microstructure of this alloy system (Cu–Zn) consists of $\alpha + \beta$ phases; α-phase is the Cu solid solution with Zn (possessing a face-centered-cubic (fcc) lattice), while β-phase is the ordered non-stoichiometric intermetallic compound CuZn (possessing a body-centered-cubic (bcc) lattice). Lead particles are dispersed preferentially, as a separate phase, in the α/β interface areas as high surface energy sites. Lead particle average size (mean diameter), which does not vary significantly between the two examined alloys, was equal to 0.95 and 0.90 μm for CuZn39Pb3 and CuZn36Pb2As, respectively. The micrographs presented in Fig. 1 illustrate that the phase structure of the brass alloys consisted of a mixture of α- and β-phases. Dark areas correspond to β-phase, while light areas correspond to α-phase, as illustrated by bright-field illumination. The CuZn39Pb3 alloy contains a higher percentage of β-phase (~35% area fraction) compared to CuZn36Pb2As (~5% area fraction). A higher magnification SEM micrograph showing a typical $\alpha + \beta$ phase structure of CuZn39Pb3 alloy, together with segregation of lead at interface boundaries, is shown in Fig. 2. The main microstructural parameters, such as β-phase content and mean particle size, assessed by image analysis software, are listed in Table 2. In addition to alloy chemical composition, the phase structure for these alloys depends on casting and hot working conditions, mainly casting temperature, casting speed, extrusion temperature, and cooling rate. Lead particle size and distribution is primarily affected by casting and solidification conditions, while the phase microstructure (volume fraction of β-phase, grain size) is influenced mainly by hot extrusion conditions (e.g., temperature, extrusion ratio, extrusion speed which

Table 1 Chemical composition and comparison to the specification limits for CuZn39Pb3 and CuZn36Pb2As rods (wt.%)

Rod/Alloy Standard	Cu	Fe	Sn	Pb	Al	Ni	As	Zn
CuZn39Pb3 rod	57.7	0.15	0,16	3.1	0,002	0,06	…	Rem
EN12164 (CuZn39Pb3 alloy —CW614N)	57–59	0.3 max	0.3 max	2.5–3.5	0.05 max	0.3 max	…	Rem
CuZn36Pb2As rod	61.6	0.01	0.01	2.1	…	0.003	0.09	Rem
EN12164 (CuZn36Pb2As alloy —CW602N)	61–63	0.3 max	0.1 max	1.7–2.8	0.05 max	0.1 max	0.02–0.15	Rem

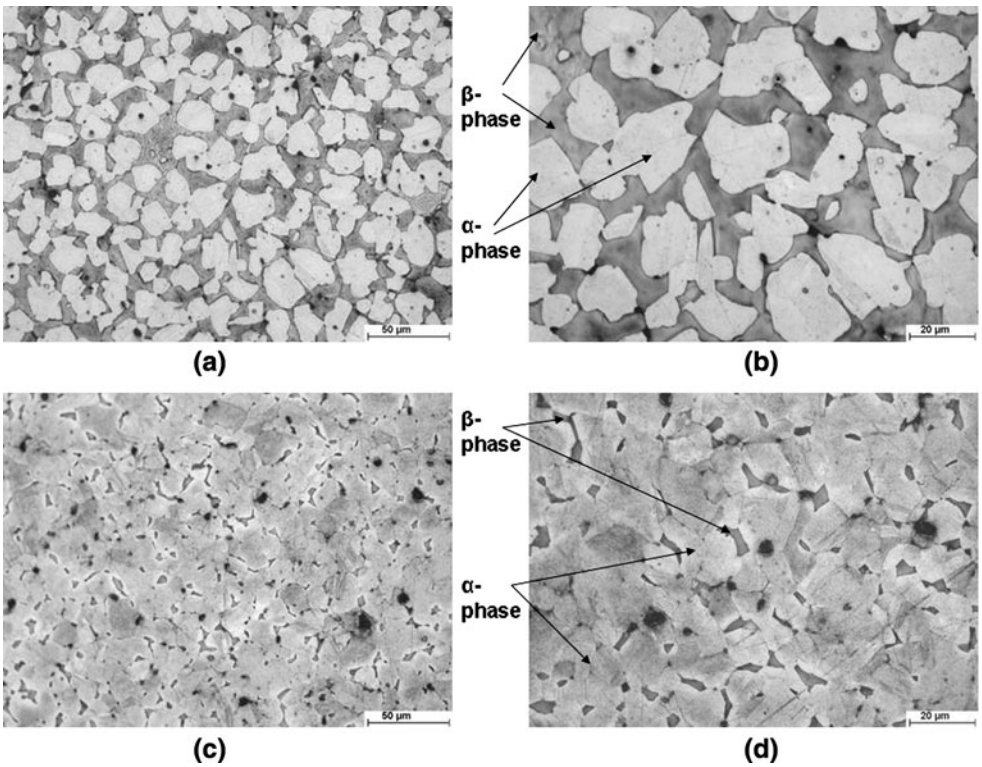

Fig. 1 Optical micrographs showing the phase structure of transverse sections: **a** CuZn39Pb3 brass rod, **b** detail of (**a**), **c** CuZn36Pb2As brass rod, **d** detail of (**c**)

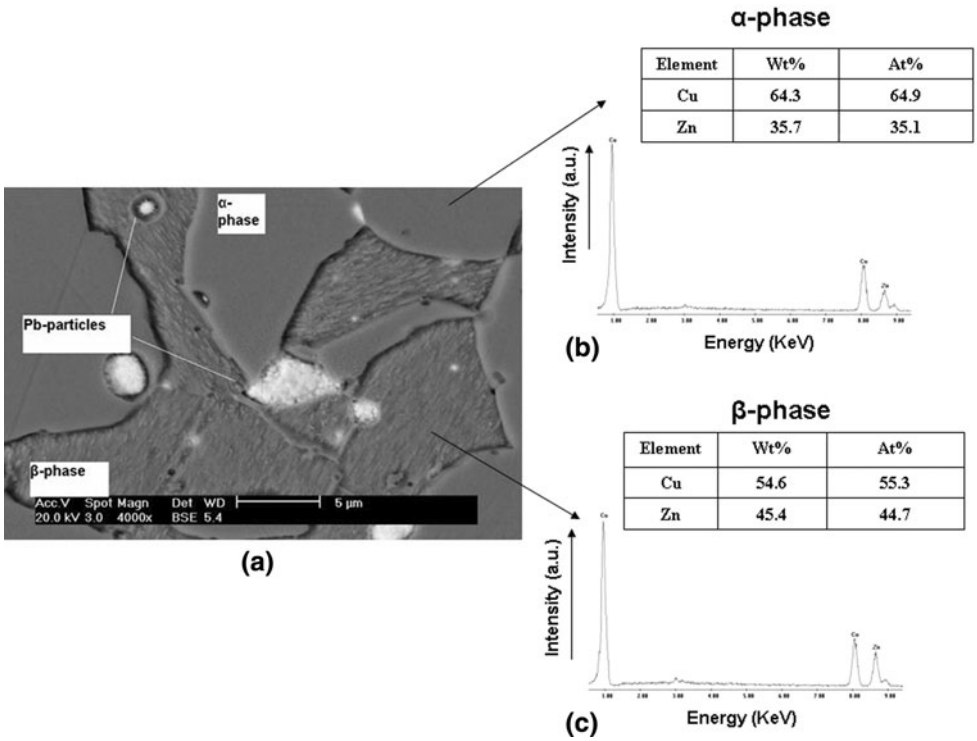

Fig. 2 **a** SEM micrograph (BSE imaging) of a characteristic area of a CuZn39Pb3 brass rod showing the phase structure at higher magnification, EDS spectrum of **b** α-phase area and **c** β-phase area

also affects the strain rate, and cooling rate). The influence of extrusion process conditions on the phase structure is reviewed by several researchers, see for example [5].

Machinability in these alloys is substantially improved by the presence and uniform distribution of fine size lead particles, since they serve as a chip-breaking constituent,

impairing chip ductility and enhancing lubricity at the tool–workpiece interface [1, 2]. Moreover, the presence of β-phase lowers the overall ductility of the alloy facilitating the segmentation of machining chips [1, 4]. β-phase also exhibits a characteristic plate-like morphology, which could be considered beneficial for chip-fracturing during machining, improving further machinability properties [2, 4].

Hardness and Tensile Properties

Vickers hardness testing showed an average hardness equal to 145 HV for CuZn39Pb3, much higher than that of alloy CuZn36Pb2As, which exhibited a mean hardness value equal to 115 HV. Alloy CuZn39Pb3 exhibited higher yield strength (350 vs. 230 MPa) and ultimate tensile strength (480 vs. 370 MPa) but lower uniform elongation (20 vs. 30%) and total elongation (24 vs. 39%), as compared to alloy CuZn36Pb2As (see Fig. 3; Table 2). Macroscopic images of top and side views of the tensile fractures are shown in Fig. 4. The reduction of area (Z) is also higher in CuZn36Pb2As alloy (55%) as compared to CuZn39Pb3 alloy (35%), see Figs. 3 and 4. CuZn36Pb2As exhibits a macroscopically ductile, fibrous fracture surface. This indicates that non-uniform elongation, characterized by the occurrence of section thinning (necking), advanced to a

Table 2 Mechanical properties and microstructure of CuZn39Pb3 and CuZn36Pb2As alloy rods

Rod alloy	Mechanical properties (a)							Microstructure (b)	
	0.2% Yield strength $R_{p0.2}$, MPa	Ultimate tensile strength R_m, MPa	Uniform elongation Ag, % (elongation reached at the maximum load)	Total elongation A50, %	Reduction of area Z, %	Vickers hardness HV_1 (values taken at midway)	Impact energy kV, J	Beta phase fraction β, %	Mean Pb particle size, µm
CuZn39Pb3	350	480	20	24	35	145	13	35	0.95
CuZn36Pb2As	230	370	30	39	55	115	30	5	0.90

(a)Obtained as the average of three independent measurements, variation was <2%

(b)Average beta phase area fractions and Pb particle size were extracted following three independent fields measurements at 200× and 500× original magnifications, respectively

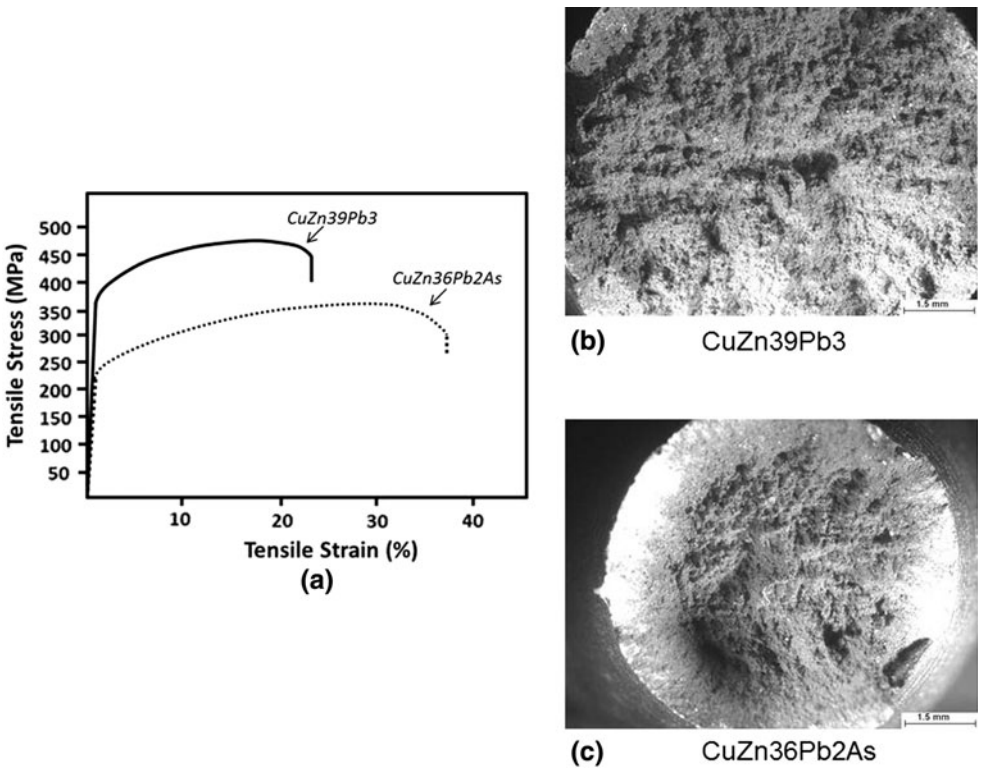

Fig. 3 **a** Representative curves presenting the evolution of tensile stress–tensile strain and stereomicrographs of the fracture surfaces of **b** CuZn39Pb3 brass rod and **c** CuZn36Pb2As brass rod

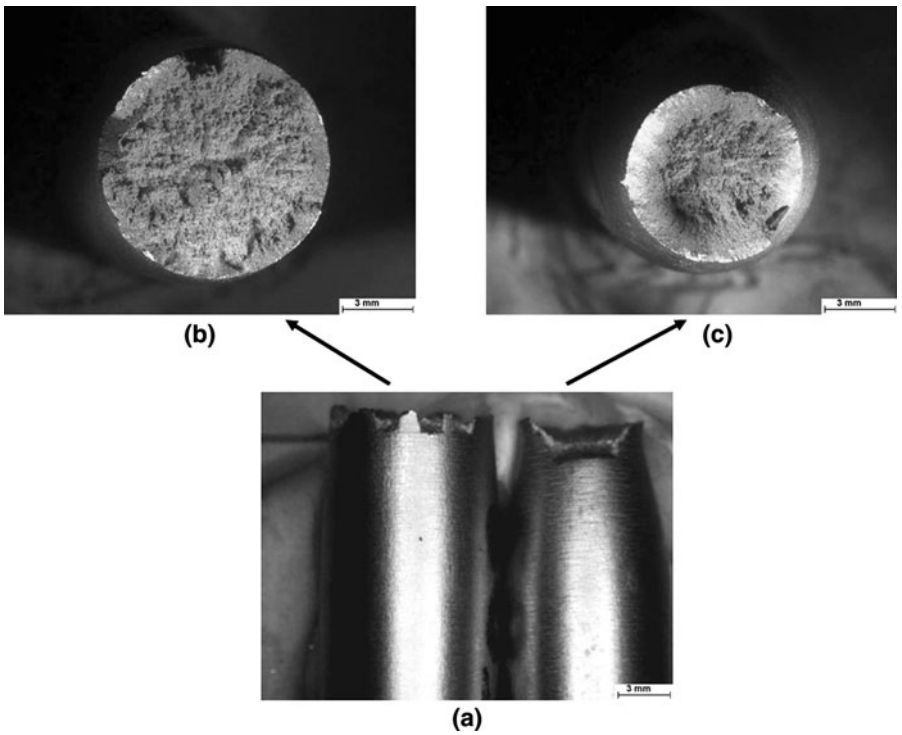

Fig. 4 **a** Optical stereomicrograph of the side views of the tensile samples after fracture and optical stereomicrographs showing the fracture surface of **b** CuZn39Pb3 brass rod and **c** CuZn36Pb2As brass rod. Note the higher reduction of area and shear lips produced in case of tensile fracture of CuZn36Pb2As brass rod

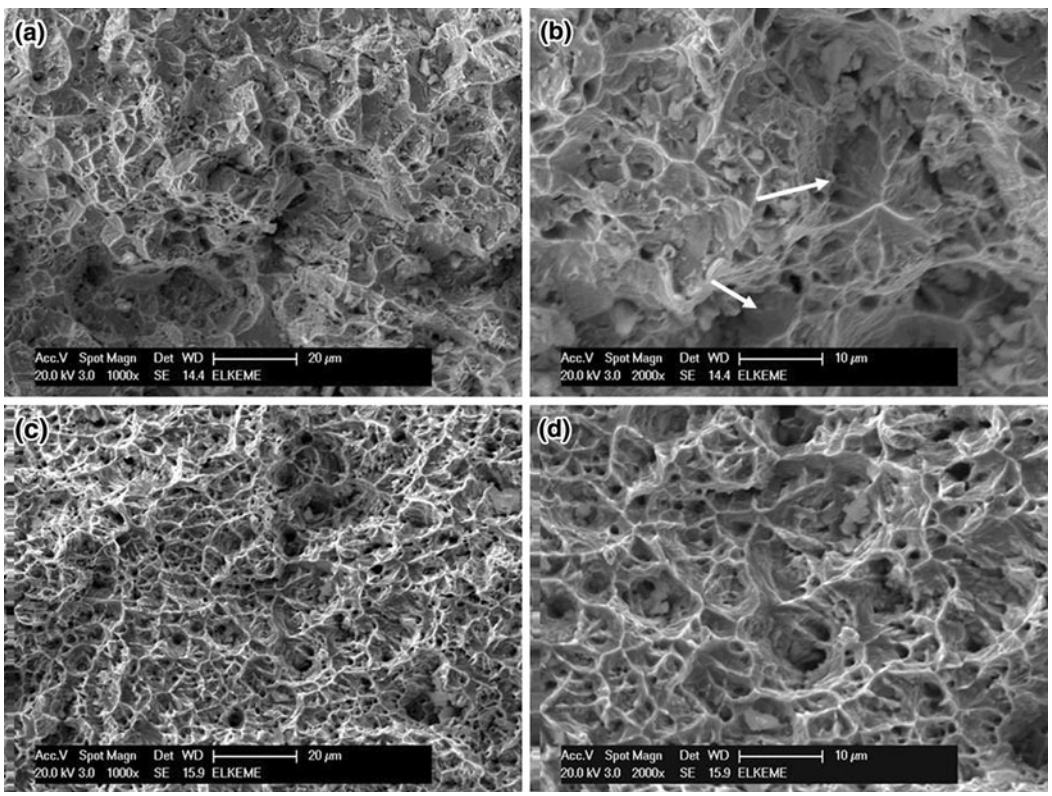

Fig. 5 SEM micrographs showing tensile fracture surface features of **a** CuZn39Pb3 brass rod, **b** detail of (**a**) at higher magnification, **c** CuZn36Pb2As brass rod, **d** detail of (**c**) at higher magnification. Note the presence of planar facets (indicated by the *arrows* in **b**) in CuZn39Pb3 fracture surface which likely constitute quasi-cleavage fractures

higher extent in case of CuZn36Pb2As alloy. Higher reduction of area as a result of greater non-uniform plastic deformation is shown by the corresponding post-necking strain outlined in the respective stress–strain curves plotted during tensile testing (Fig. 3a, c). The uniform, almost single-phase structure (≥95% fraction of α-phase) of the CuZn36Pb2As alloy seems more resistant, compared to CuZn39Pb3 alloy, to incipient necking formation under triaxial stress state, thereby extending the corresponding post-uniform plastic deformation.

Tensile Fracture Modes

The topographic features of tensile fracture surfaces of brass alloys were studied at higher magnification by means of scanning electron microscopy. Typical fractographic aspects of the tensile fracture surfaces are shown in Fig. 5. A mixed-mode fracture combining dimple formation and planar faceted fracture, likely induced by a quasi-cleavage process, is identified in the case of CuZn39Pb3 alloy (Fig. 5a, b). On the other hand, CuZn36Pb2As alloy demonstrated a typical ductile fracture consisting of fine equiaxed dimples (Fig. 5c, d). The limited total elongation and reduction of area observed in the CuZn39Pb3 alloy could be attributed to the relevant fracture mechanism, which involves the development of quasi-brittle cleavage facets (Fig. 6a). The formation of cleavage rupture, observed sporadically in isolated areas of the fracture surface, could be connected with the non-uniform phase structure and probably due to the presence of the harder β-phase which possesses lower plasticity than α-phase. Microvoid nucleation takes place at high stress concentration sites (e.g., inherent second-phase particles, inclusion clusters) while their growth proceeds up to a critical size, where the remaining interconnection ligaments are subjected to shear and unstable crack propagation occurs. Emerging shear fractures, expressed through transgranular cleavage, restrict overall plasticity, minimizing, therefore, the total elongation and reduction of area. A schematic diagram of this proposed fracture mechanism is presented in Fig. 6(b).

Impact Properties

Impact testing, employing the standard Charpy V-Notch method and performed at ambient temperature, showed significantly higher toughness for the CuZn36Pb2As alloy (30 J) compared to the CuZn39Pb3 alloy (13 J), see Table 2 and Fig. 7. Diagrams presented in Fig. 7(b) and (d) show the temporal variation of load and absorbed energy plotted during impact test, while the fracture surfaces of CuZn39Pb3 and CuZn36Pb2As are illustrated in Fig. 7(a) and (c), respectively.

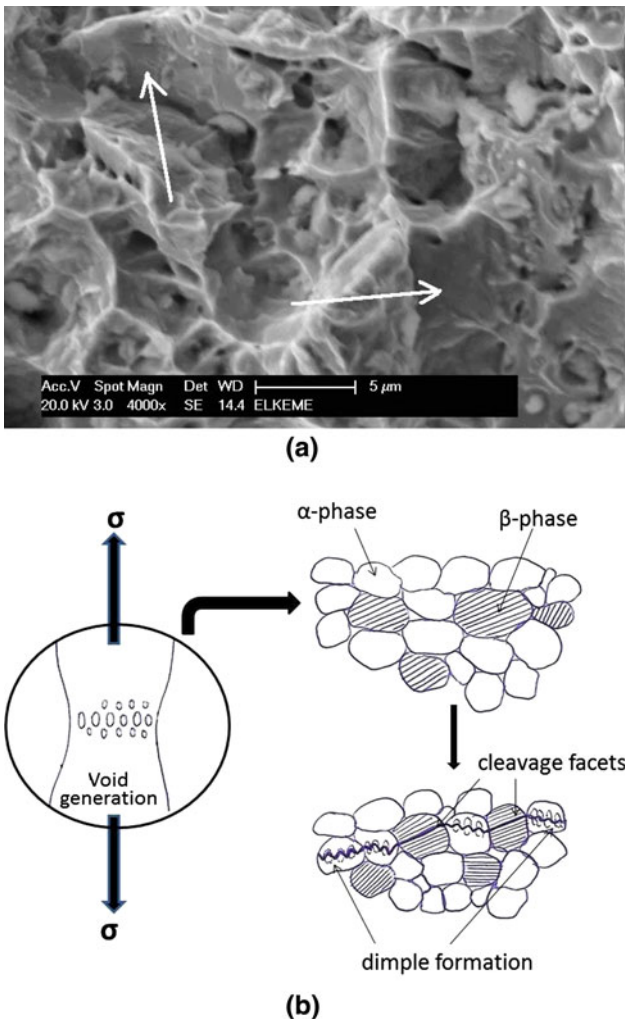

Fig. 6 **a** Higher magnification SEM micrograph of the tensile fracture surface of CuZn39Pb3 indicating the presence quasi-cleavage facets. **b** Simple schematic showing the proposed mixed fracture mode evolution; microvoid growth and coalescence ending up to dimple ductile fracture while cleavage fracture occurred preferentially through β-phase crystals. For simplicity purposes, microplasticity of α-phase crystals is not shown in the microstructure sketch

Impact Fracture Modes

Moderate distortion of the cross section is depicted by CuZn36Pb2As (Fig. 7c), indicating the higher degree of plastic deformation imposed during impact. Crack initiation is located at the notched area, as manifested by the convergent chevron marks while crack front advances toward the front direction is marked in Fig. 8. Fracture surfaces of both the alloys present slightly discerned differences; the fracture surface of CuZn39Pb3 consisted mainly of fine "shear" dimples combined with planar facets (Fig. 9a, b), while fracture surface of CuZn36Pb2As consisted almost exclusively of coarser dimples consistent with the higher plastic deformation accommodated by this alloy (Fig. 9c, d). The presence of elongated non-equiaxed

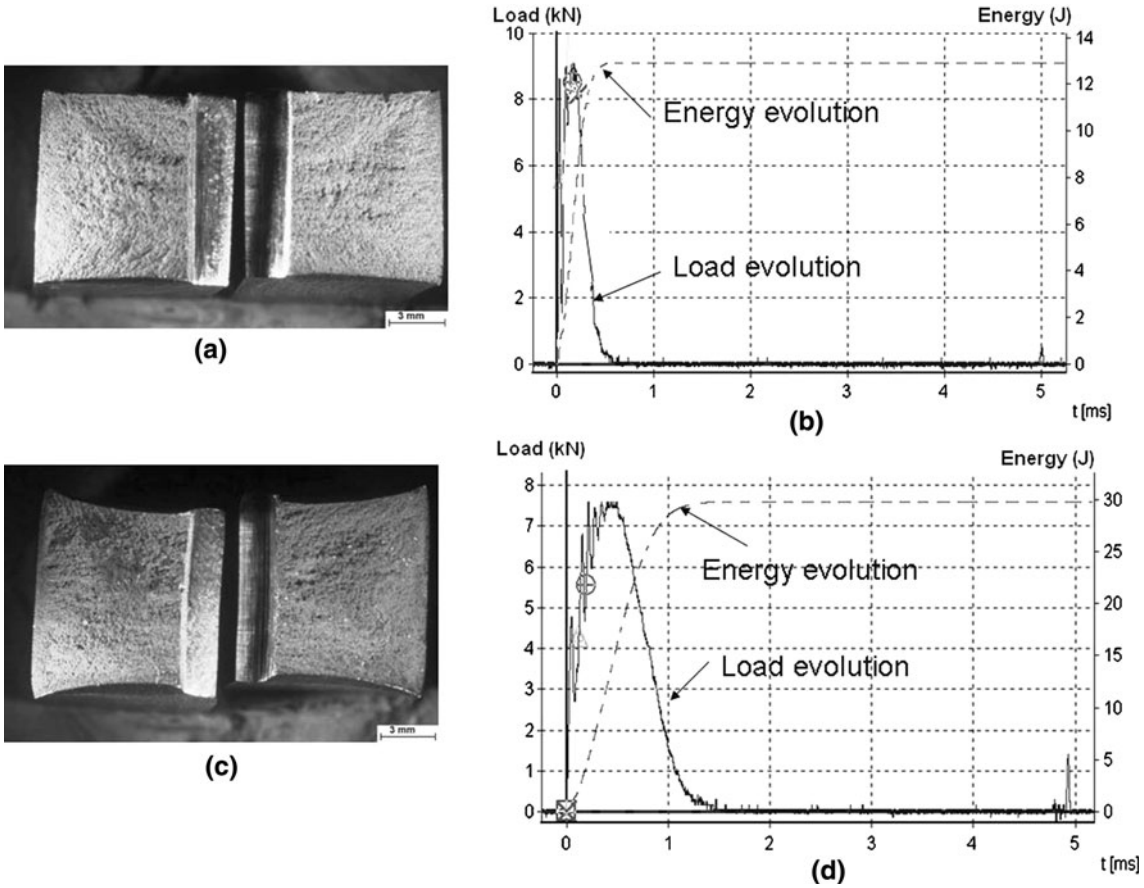

Fig. 7 **a** Fracture surfaces and **b** temporal evolution of load and absorbed energy during impact test of CuZn39Pb3 brass rod and **c** fracture surfaces and **d** temporal evolution of energy and force during impact of CuZn36Pb2As brass rod. *Dashed lines* indicate the absorbed energy evolution while continuous lines indicate load evolution

dimples is an indication of final ductile tearing under the application of shear stresses. As reported in the investigation of tensile fractures, planar facets are related to the occurrence of low energy quasi-cleavage brittle fracture mechanism which accelerates final failure and minimizes total plastic deformation and energy absorption. The higher magnification SEM micrograph shown in Fig. 10 indicates the presence of quasi-cleavage steps formed in CuZn39Pb3 alloy during impact testing.

Conclusions

In this study, the mechanical behavior of alloy CuZn39Pb3, a high machinability alloy, was compared with alloy CuZn36Pb2As, an alloy with lower machinability, but high dezincification resistance. The results of the microstructure analysis, mechanical testing, and fracture surface examination lead to the following conclusions:

1. The CuZn39Pb3 alloy exhibited a significantly higher fraction of β-phase compared to the CuZn36Pb2As alloy (35 vs. 5%, respectively). Higher lead content and β-phase fraction contribute mainly to the higher machinability possessed by the CuZn39Pb3 alloy compared to the CuZn36Pb2As alloy.
2. Compared to As-containing alloy, CuZn39Pb3 shows:
   a. Substantial increase of 0.2% yield strength $R_{p0.2}$ (370 vs. 230 MPa) and ultimate tensile strength R_m (480 vs. 370 MPa) and
   b. A decrease of total elongation A50 (24 vs. 39%), reduction of area Z (35 vs. 55%) and impact energy (13 vs. 30 J).
3. Tensile failure of the CuZn36Pb2As alloy exhibited a typical dimpled fracture surface due to the microvoid growth and coalescence processes, while the CuZn39Pb3 alloy exhibited a mixed fracture mode, combining dimpled areas with isolated low ductility planar facets.
4. Differences encountered in impact fracture modes between the two brass alloys are consistent with the variation in absorbed energy and section distortion

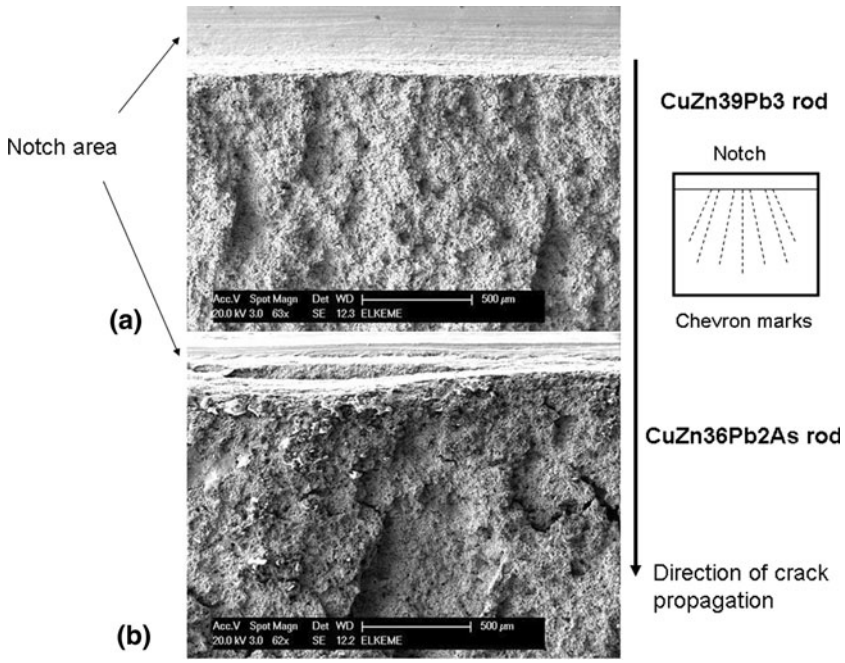

Fig. 8 SEM micrographs showing low-magnification surface topography of the impact fracture area close to the notch, indicating the presence of chevron-rays and elucidating the direction of crack propagation

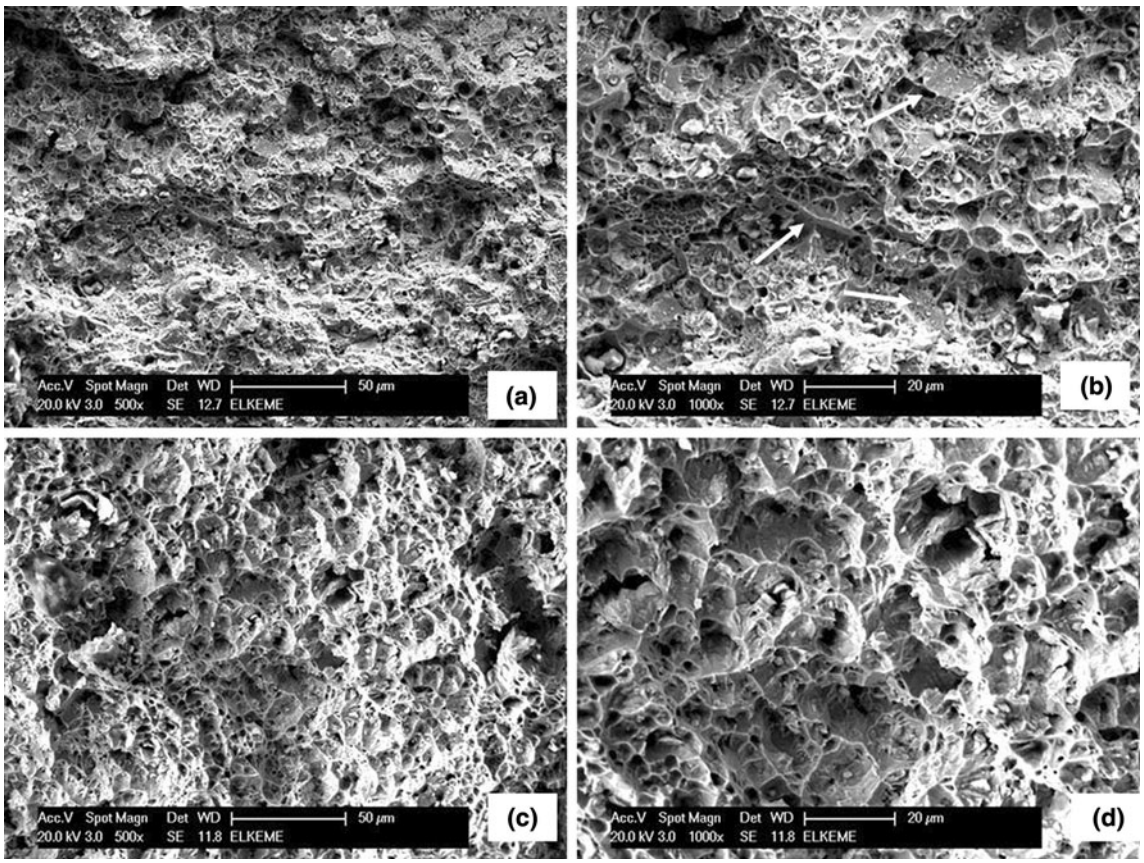

Fig. 9 SEM micrographs showing impact fracture surface features of **a** CuZn39Pb3 brass rod, **b** detail of (**a**) at higher magnification, **c** CuZn36Pb2As brass rod, **d** detail of (**c**) at higher magnification. Note the presence shear dimples and planar facets (indicated by the *arrows* in **b**) in CuZn39Pb3 fracture surface which likely constitute quasi-cleavage fractures

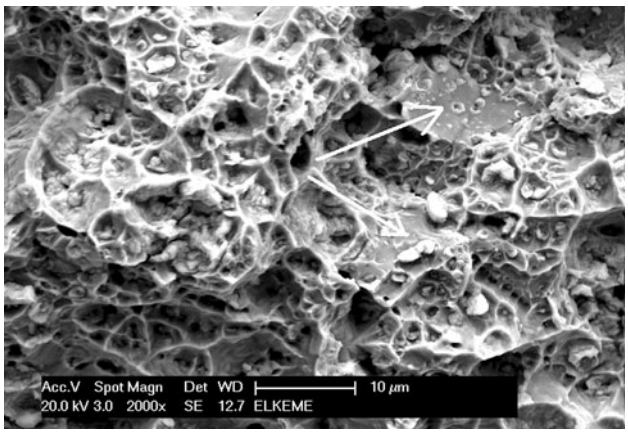

Fig. 10 Higher magnification SEM micrographs depicting the presence of quasi-cleavage facets located on the impact fracture surface of CuZn39Pb3 brass rod

observed. More specifically, the CuZn36Pb2As alloy demonstrates almost uniform fracture mode consisting of fine shear dimples, while the CuZn39Pb3 alloy is characterized by the presence of isolated quasi-cleavage facets, which are assumed to suppress the overall plasticity expressed as strain energy.

5. Further research is suggested to determine and validate in a more comprehensive manner the role of size and distribution of β-phase on the incurred failure mechanism.

References

1. G. Pantazopoulos, Leaded brass rods C38500 for automatic machining operations: a technical report. J. Mater. Eng. Perform. **11**, 402–407 (2002)
2. A.I. Toulfatzis, G.J. Besseris, G.A. Pantazopoulos, C. Stergiou, Characterization and comparative machinability investigation of extruded and drawn copper alloys using non-parametric multi-response optimization and orthogonal arrays. Int. J. Adv. Manuf. Technol. **57**, 811–826 (2011)
3. P. Garcia, S. Rivera, M. Palacios, J. Belzunce, Comparative study of the parameters influencing the machinability of leaded brasses. Eng. Fail. Anal. **17**, 771–776 (2010)
4. G. Pantazopoulos, A. Vazdirvanidis, Characterization of the microstructural aspects of machinable α-β brass. Microsc. Anal. **22**(5), 13–16 (2008)
5. K. Holler, B. Reetz, K.B. Müller, A. Pyzalla, W. Reimers, Microstructure and properties of hot extruded brass CuZn40Pb2. Mater. Sci. Forum **426–432**, 3667–3672 (2003)
6. "Fractography", ASM Handbook, Vol. 12, ASM International, Materials Park, OH, 1992
7. D. Hull, *Fractography, observing, measuring and interpreting fracture surface topography* (Cambridge University Press, Cambridge, 1999)
8. S.P. Lynch, S. Moutsos, A brief history of fractography. J. Fail. Anal. Prev. **6**(6), 54–69 (2006)
9. G.A. Pantazopoulos, Damage assessment using fractography as failure surface evaluation: applications in industrial metalworking machinery. J. Fail. Anal. Prev. **11**(6), 588–594 (2011)
10. G. Pantazopoulos, A review of defects and failures of brass rods and related components. Pract. Fail. Anal. **3**(4), 14–22 (2003)
11. G. Pantazopoulos, A. Vazdirvanidis, Failure analysis of fractured leaded-brass (CuZn39Pb3) extruded hexagonal rod. J. Fail. Anal. Prev. **8**(3), 218–222 (2008)